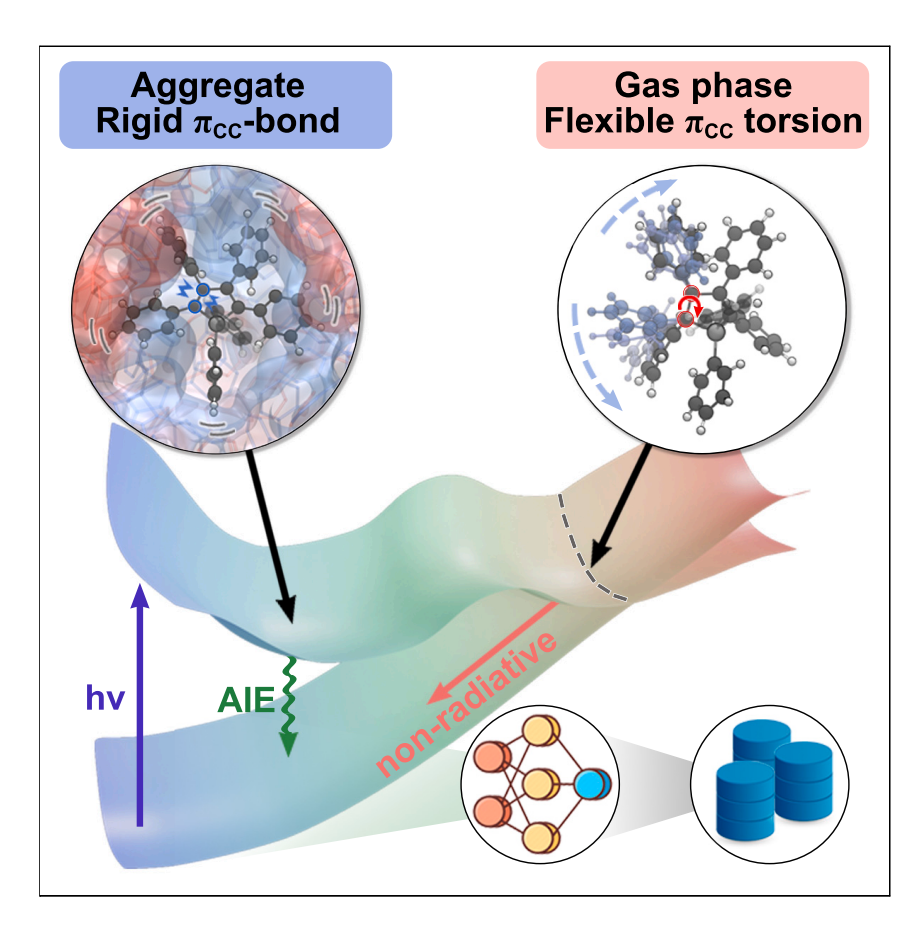




## **Article**

# Machine learning photodynamics uncover blocked non-radiative mechanisms in aggregation-induced emission



Multiscale ML-photodynamics enabled the excited-state dynamics simulations for AIE molecules in aggregates. The trajectories with high-fidelity atomistic resolution predicted fluorescence enhancements in line with the experiments. A comprehensive survey of the non-radiative mechanisms for AIE molecules revealed that the non-radiative decay originated from the excited-state  $\pi_{\rm CC}$  torsions in the conjugated cores. The intermolecular clashes in aggregates blocked the  $\pi_{\rm CC}$  torsion to promote AIE. The new mechanistic insights pave the way toward the rational design of AIE materials.

Li Wang, Christian Salguero, Steven A. Lopez, Jingbai Li

s.lopez@northeastern.edu (S.A.L.) lijingbai@szpu.edu.cn (J.L.)

### Highlights

Machine learning accelerated photodynamics simulations for molecular aggregates

 $\pi_{\text{CC}}\text{-bond}$  torsions lead to non-radiative decay of AIE molecules

Intermolecular steric clashes block the  $\pi_{\text{CC}}$  torsions to promote AIE



Wang et al., Chem 10, 1–16 July 11, 2024 © 2024 Elsevier Inc. All rights reserved.

https://doi.org/10.1016/j.chempr.2024.04.017

Chem



### **Article**

# Machine learning photodynamics uncover blocked non-radiative mechanisms in aggregation-induced emission

Li Wang,<sup>1</sup> Christian Salguero,<sup>2</sup> Steven A. Lopez,<sup>2,\*</sup> and Jingbai Li<sup>1,3,\*</sup>

### **SUMMARY**

Aggregation-induced emission (AIE) is a photophysical phenomenon in which weakly luminescent organic chromophores become strongly luminescent in aggregate. The reduced non-radiative decay in aggregates is often cited as the explanation of the AIE. However, the mechanism of competing non-radiative decay pathways is not resolved due to the lack of excited-state structural information in the time-resolved experiments and prohibitively expensive quantum mechanical calculations for photodynamics simulations. We investigated the excitedstate dynamics of classic AIE molecules in aggregate, hexaphenylsilole (HPS), tetraphenylsilole (TPS), and cyclooctatetrathiophene (COTh) with a multiscale machine learning accelerated photodynamics approach, integrating neural networks, semiempirical methods, and molecular mechanics. Our simulations predict 263-, 5-, and 12-fold fluorescence enhancement of HPS, TPS, and COTh in good agreement with the experiments (255, 3, and 12). We identified a shared non-radiative decay mechanism involving  $\pi_{CC}$  torsions in these molecules. These torsions are blocked in aggregate due to intermolecular hindrance between substituents, promoting AIE.

### **INTRODUCTION**

Organic luminescent molecules are gaining increasing interest in material science, biology, and chemistry, triggering rapid developments of organic light-emitting diodes, 1 chemosensors, 2-5 biosensors, 6,7 and bioimaging. 8-10 These molecules can emit light because they are trapped in an excited-state local minimum after photoexcitation. The excitation energy is converted back to a photon in a radiative pathway. The excitation energy can also lead to photochemical reactionaules 11 through a crossing point between the excited and the ground states, which converts the absorbed photonic energy into molecular vibrations non-radiatively. Hence, designing luminescent materials with high luminescent quantum yields should avoid this non-radiative process. However, the non-radiative processes of organic molecules are often intricate because they occur in an ultrafast timescale, and their relationship with the molecular structures is elusive due to the lack of high-fidelity structural information in experiments. Investigating the fundamental mechanistic nature of the competing radiative and non-radiative pathways is required to rationally design organic luminescent materials.

Aggregation-induced emission (AIE)<sup>12,13</sup> has provided a novel strategy for designing organic luminescent materials with reduced non-radiative processes in the last two decades.<sup>14–21</sup> The restriction of intramolecular motions (RIM) mechanism was proposed by Tang and co-workers to explain the AIE phenomena in

### THE BIGGER PICTURE

Aggregation-induced emission (AIE) provides fertile ground for the rapid development of organic luminescent materials. However, resolving the excited-state mechanisms of AIE phenomena remains a formidable challenge because of the limited resolutions of the time-resolve experiments and costly excited-state dynamics simulations of aggregates.

Here, we report our multiscale machine learning accelerated photodynamics simulations for classical AIE molecules in aggregate state. Our results reproduce the fluorescence enhancement reported in experiments and reveal that the substituents block the  $\pi_{CC}$ torsions in the conjugated cores, which significantly reduces nonradiative decay to produce AIE. The new mechanistic insights provide an atomistic understanding of the relationship between the substituents and the conjugated core in AIE phenomena, thus paving the way toward the rational design of AIE materials in a broadened chemical space.





many molecular aggregates based on chemical intuition.<sup>22-24</sup> The non-radiative decay pathways were deactivated because of the restricted intramolecular rotations (RIR) in hexaphenylsilole (HPS), 25,26 tetraphenylethylene (TPE), 27 and dimethytetraphenylsilole (DMTPS),<sup>28</sup> and the restricted intramolecular vibrations (RIV) in bidibenzo [7]-annulenylidene (BDBA) and tetrahydrobidibenzo [7]-annulenylidene (THBDBA),<sup>22</sup> as shown in Figure 1A. Later, computational studies by Blancafort and co-workers suggested that the RIM mechanism in the diphenyldibenzofulvene (DPDBF)<sup>29</sup> and DMTPS crystals hinder the  $\pi_{CC}$ -bond distortions toward the conical intersection (CI). 30 These findings extended the RIM mechanism to the restricted access to a CI (RACI)<sup>30,31</sup> theory for studying the enhanced fluorescence in molecular crystals (Figure 1B). The RIM and RACI mechanisms provide a static perspective of the non-radiative decay in AIE molecules (Figure 1C) but cannot inform the non-radiative decay rate constants and quantum yields (QYs). Shuai and co-workers developed the thermal vibration correlation function (TVCF) theory to predict QYs for AIE molecules in close agreement with experiments.<sup>32</sup> However, the TVCF theory cannot predict the non-radiative decay rate constants in non-harmonic regions (such as a peaked CI) because it employs the harmonic approximation in excitedstate potential energy surfaces (PESs). Moreover, the photoexcited molecule is substantially higher in energy than the minimum energy CI. The non-radiative decay could occur at many points along the intersection seam instead of the minimum energy CI,33 which further complicates the mechanism. This study, thus, uses state-of-the-art quantum chemical calculations and machine learning (ML) techniques to disentangle non-radiative decay mechanisms and identify the origin of the reduced non-radiative decay of aggregated AIE molecules (Figure 1D).

It remains unclear which nuclear motion(s) control(s) the non-radiative decay in AIE molecules leading to the AIE. Photodynamic simulations provide a path toward understanding the dynamical mechanism of the behavior of molecular photoexcited states, especially non-radiative decay. 36,37 These simulations are costly; they are limited to studying the excited-state dynamics of medium-sized molecules (50 atoms) in subpicosecond<sup>38</sup> because they require on-the-fly quantum mechanical (QM) calculations of the excited-state PES and nonadiabatic couplings (NACs). Most AIE molecules (e.g., HPS) require prohibitive computational costs because of their relatively complex molecular structures and relatively long excited-state lifetimes (picoseconds to nanoseconds). Moreover, the molecular aggregates feature thousands of atoms and undergo slowed non-radiative decay, which makes the photodynamics simulations computationally infeasible. A few reports explain the gasphase photodynamics of the AIE molecules; these simulations suggest that various intramolecular motions (e.g.,  $\pi_{CC}$ -bond twisting<sup>39</sup> and stretching<sup>40</sup>) are relevant to non-radiative decay mechanisms. The vast computational cost, even at the molecular level, limits the studies to relatively small molecules (e.g., TPE<sup>39</sup>) or a low-cost semiempirical QM method (e.g., the time-dependent (TD) density functional tight binding theory<sup>40</sup>).

To determine the nuclear motion(s) controlling the non-radiative decay of AIE molecules, we use ML accelerated photodynamics simulations developed by our group and others (e.g., Dral and Barbatti, <sup>41</sup> Westermayr and Marquetand, <sup>42</sup> and Li and Lopez <sup>43</sup> to simulate non-radiative processes in molecular aggregates. The ML-photodynamics simulations showed fast and accurate predictions in studying the excited-state dynamics of various molecules up to nanoseconds. <sup>44,45</sup> For simulating molecular aggregates, we expanded the ML-photodynamics approach into multiscale by combining the neural networks (NNs) trained with QM calculations, semiempirical (GFN0-xTB), and molecular mechanics (GFN-FF) calculations (details

https://doi.org/10.1016/j.chempr.2024.04.017

<sup>&</sup>lt;sup>1</sup>Hoffmann Institute of Advanced Materials, Shenzhen Polytechnic University, Shenzhen, Guangdong 518055, China

<sup>&</sup>lt;sup>2</sup>Department of Chemistry and Chemical Biology, Northeastern University, Boston, MA 02115, USA

<sup>&</sup>lt;sup>3</sup>Lead contact

<sup>\*</sup>Correspondence:

s.lopez@northeastern.edu (S.A.L.), lijingbai@szpu.edu.cn (J.L.)





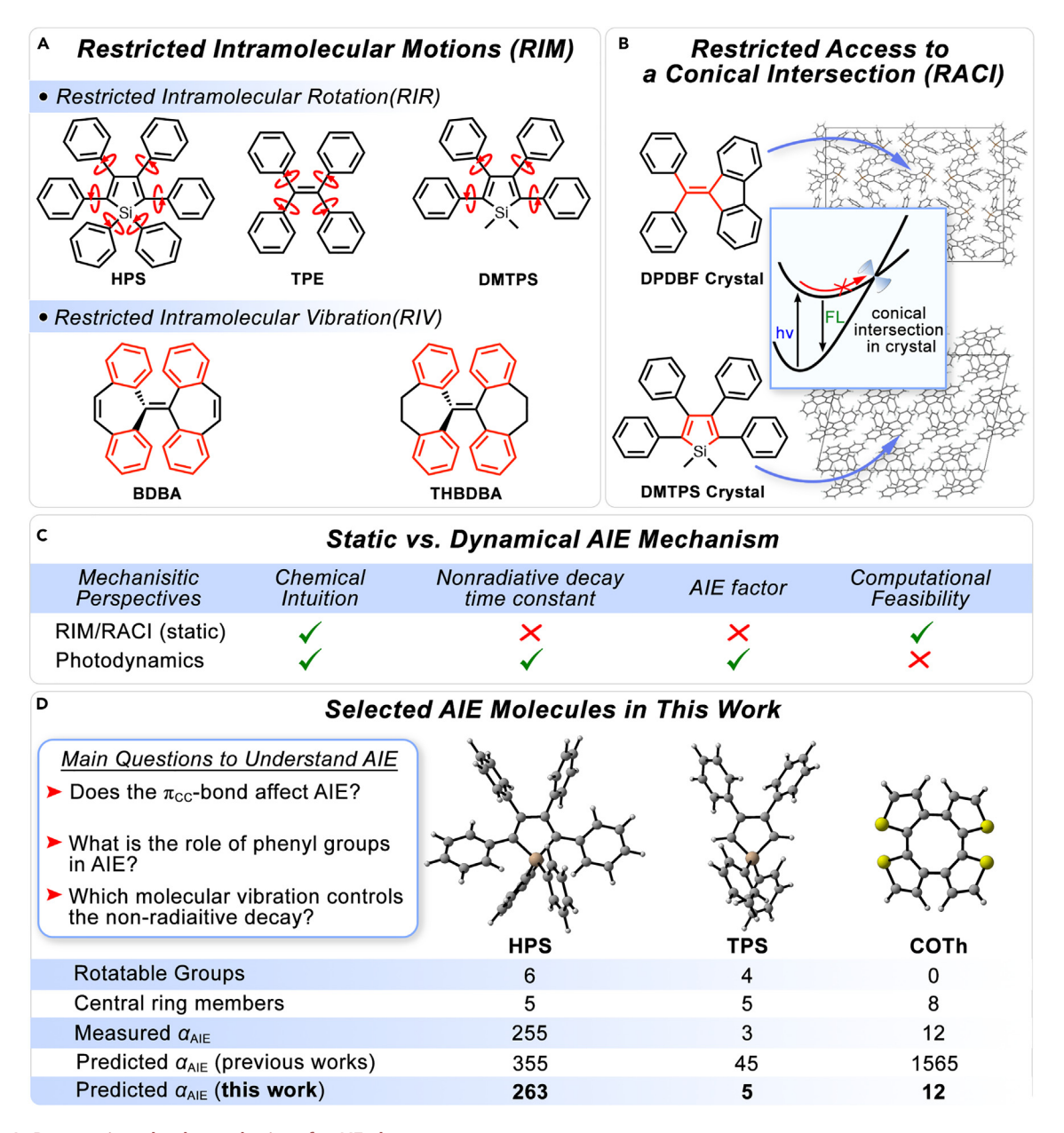


Figure 1. Progress in molecular mechanisms for AIE phenomena

(A) The schematic illustration of the restricted intramolecular motion (RIM) mechanism, including the restricted intramolecular rotation (RIR) for HPS, <sup>25,26</sup> TPE, <sup>27</sup> DMTPS, <sup>28</sup> and the restricted intramolecular vibration (RIV) for BDBA and THBDBA. <sup>22</sup>

- (B) The schematic illustration of the restricted access to a conical intersection (RACI) mechanism for **DPDBF** and **DMTPS** crystals. The restricted motions of the phenyl groups and  $\pi_{CC}$ -bond are highlighted with red arrows and bonds for (A) and (B).
- (C) The comparison between the static and dynamical perspectives of the non-radiative mechanism in AIE phenomena.
- (D) The main mechanistic questions addressed in this work and the selected AIE molecules with the fluorescence enhancement,  $\alpha_{AIE}$ . Previous works predicted the  $\alpha_{AIE}$  of HPS, <sup>34</sup> TPS, <sup>34</sup> and COTh <sup>35</sup> based on the static calculations in the gas-phase and crystal structures.

are in Multiscale approach). We studied three prototypical AIE molecules, HPS, TPS, and cyclooctatetrathiophene (COTh), to identify the role of intramolecular motions in the non-radiative decay mechanisms in different classes of AIE molecules (Figure 1D). The ML-photodynamics reproduced the experimental enhancement of the fluorescence QYs (i.e., AIE factors,  $\alpha_{\rm AIE}$ ) in good agreement with the experiments. The trajectories revealed similar  $\pi_{\rm CC}$  torsions in the conjugated core,





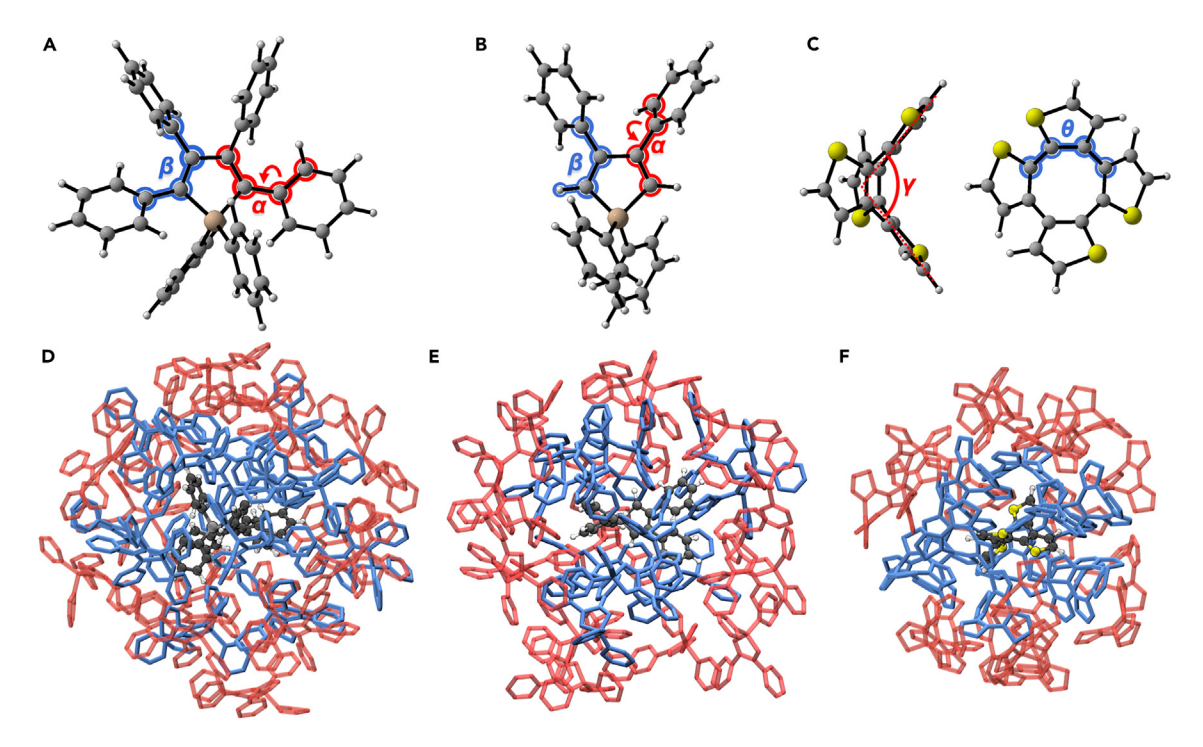


Figure 2. Gas-phase and molecular aggregate models

(A and B) Illustrations of the representative phenyl group rotation angle ( $\alpha$ ) and silole-core  $\pi_{CC}$  torsion angle ( $\beta$ ) in HPS (A) and TPS (B). (C) The inversion angle ( $\gamma$ ) and COTh-core  $\pi_{CC}$  torsion angle ( $\theta$ ) in COTh (C).

(D–F) Snapshots of the HPS, TPS, and COTh aggregate models. The dynamics of the excitation core, inner shell (blue), and outer shell (red) are modeled with NNs, GFN0-xTB, and GFN-FF methods in a three-layer ONIOM scheme.

contributing to the non-radiative decay despite the distinct core structures and varying number of substituents in HPS, TPS, and COTh. Our findings provide new mechanistic insights beyond the RIM and RACI theories and demonstrate a possible strategy to enhance the fluorescence of organic molecules for the rational design of AIE molecules.

### **RESULTS AND DISCUSSION**

### Gas-phase and aggregate-state models

The experiments measured the fluorescence QYs of HPS, TPS, and COTh from a dilute solution to a high concentration by increasing the water fraction in organic solutions to investigate AIE phenomena. We approximate the dilute solution as a gas-phase simulation and the high concentration as a molecular aggregate for the excited-state dynamics. The gas-phase and aggregate models correspond to the solutions with 0% and 100% water fractions, respectively. These conditions enabled us to determine the restricted motions responsible for the reduced non-radiative process (i.e., the increased AIE intensity). For the gas-phase simulations, we used Wigner sampling to generate 1,500 initial conditions for HPS, TPS, and COTh at the zero-point energy level. We defined the geometrical parameters to characterize the gas-phase intramolecular motions.  $\alpha$  and  $\beta$  represent the phenyl group rotations and the silole-core  $\pi_{\rm CC}$ -bond torsions of HPS (Figure 2A) and TPS (Figure 2B).  $\gamma$  and  $\theta$  measure the inversion angle and the COTh-core  $\pi_{\rm CC}$ -bond torsions of COTh (Figure 2C). Detailed interpretations of the geometrical parameters are in gas-phase ML-photodynamics.

To generate the aggregate models, we first pruned the HPS, TPS, and COTh supercells into a central molecule with two shells to generate the aggregates. The central





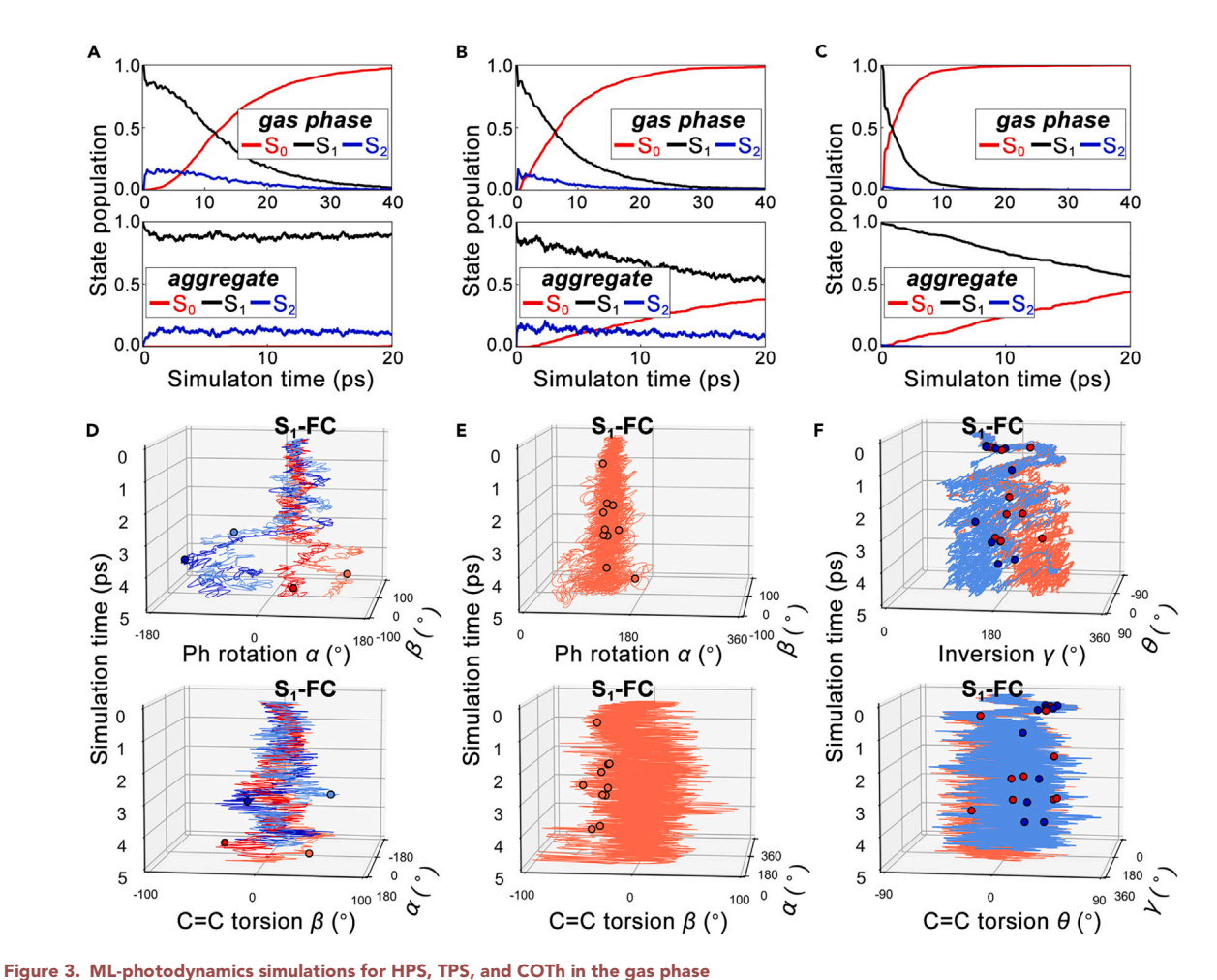
molecule was replaced with the gas-phase Wigner-sampled structures, and the molecules comprising the shells were relaxed with molecular dynamics by the GFN0-xTB and GFN-FF methods. Previous studies on HPS aggregates suggested the AlE observed for the central molecule is independent of aggregate-solvent interactions. He refore, we employed an external spherical constraining potential to mimic the solute-solvent interactions forming the aggregates. Figures 2D–2F illustrate one of the 500 initial conditions for the HPS, TPS, and COTh aggregate models. The average densities of the aggregate models were 1.01, 0.97, and 1.27 g·cm<sup>-3</sup>, respectively, in line with the simulated amorphous aggregates in the previous report. Detailed protocols for aggregate-state model preparation are in aggregate models.

The experiments and TD- $\omega$ B97XD/cc-pVDZ calculations (Table S1) suggest that HPS, TPS, and COTh are promoted to their respective S<sub>1</sub>-Franck-Condon (FC) points (Figure S1) upon photon absorption. The subsequent non-radiative decay occurs when the molecular trajectories approach the S<sub>1</sub>/S<sub>0</sub>-Cls. Simulating the excited-state dynamics toward S<sub>1</sub>/S<sub>0</sub>-Cls requires multireference QM methods, such as complete active space self-consistent field (CASSCF) with second-order perturbative corrections (CASPT2). However, neither CASPT2 nor CASSCF methods are computationally feasible for large molecules like HPS and TPS. The CASSCF energy calculations for HPS using the minimal basis set (ANO-S-MB) required 4 h on our high-performance computer, which would spend 18 years to simulate the non-radiative decay of HPS in 20 ps, according to the rate constant (2.53  $\times$  10<sup>10</sup> s<sup>-1</sup>) reported by Shuai and co-workers.<sup>34</sup> As such, we turned to NNs to accelerate the excited-state dynamics for HPS, TPS, and COTh in the gas phase and aggregate.

To generate the training data for the NNs, we interpolated the structures from the  $S_1$ -FC points to the  $S_1/S_0$ -Cls and compute the energies and gradients of the  $S_0$ ,  $S_1$ , and  $S_2$  states. These data can describe the dominating  $S_1 \rightarrow S_0$  transitions and possible transitions between  $S_1$  and  $S_2$ . The training data were computed with the TD- $\omega$ B97XD/cc-pVDZ calculations because the CASSCF calculations overestimate the excitation energies due to the poor quality of the affordable minimal basis sets and the omission of dynamical electron correlation. The TD- $\omega$ B97XD/cc-pVDZ calculations produced comparable geometries, g (gradient difference), and g (nonadiabatic coupling) vectors to the CASSCF reference, except for missing the dimensionality of the branching plane. The discrepancy on the PESs became less significant when leaving the  $S_1/S_0$ -MECIs (e.g.,  $S_1-S_0$  energy gap  $S_1$ 0.3 eV) because the  $S_1/S_0$ -MECIs were sloped and the gradient differences dominated the molecular vibrations to lift the  $S_1/S_0$  degeneracy. Thus, the training set removes the data points at the  $S_1/S_0$ -MECIs to exclude inaccurate PES data.

We used the curvature-driven time-derivative coupling (kTDC) approach  $^{49,50}$  to approximate the NACs for Tully's fewest switches surface hopping (FSSH) $^{51,52}$  calculations. The kTDC approach showed almost identical results to the ground-truth NACs when the  $S_1$ – $S_0$  energy gap < 0.1 eV.  $^{53,54}$  In our ML-photodynamics simulations, most  $S_1$ – $S_0$  transitions of HPS, TPS, and COTh (94.7%–97.0%) were predicted with an  $S_1$ – $S_0$  energy gap > 0.3 eV, where the kTDC overestimated the ground-truth NACs by 2–10 times (Figure S5). Thus, the ML-photodynamics simulations will overestimate the  $S_1$ – $S_0$  non-radiative decay rate constants. Nevertheless, the predictions of the AIE factor are unlikely to be affected as they depend on the ratio between the non-radiative decay rate constants in the gas phase and aggregate (aggregate ML-photodynamics for details).





(A–C) Comparisons of the gas-phase and the aggregate-state electronic state population dynamics of HPS, TPS, and COTh in the first 40 ps. (D and E) Plots for the selected HPS, TPS, and COTh trajectories from their  $S_1$ -FC region to the  $S_1$ / $S_0$  surface hopping points (black circles) for the first 5 ps gas-phase ML-photodynamics simulations. (D) The  $\alpha$ -front view and  $\beta$ -front view of the HPS trajectories are colored by the  $S_1$ / $S_0$  surface hopping points where  $\alpha$  < 0°(red) and  $\alpha$  > 0° (blue). (E) The  $\alpha$ -front view and  $\beta$ -front view of the selected gas-phase TPS trajectories highlight the preferred  $S_1$ / $S_0$ 

(F) The  $\gamma$ -front view and  $\theta$ -front view of the gas-phase COTh trajectories illustrate the reversion ( $\gamma < 180^{\circ}$ ) and inversion ( $\gamma > 180^{\circ}$ ) of COTh.

### **Predictions of the AIE factors**

surface hopping points where  $\beta < 0^{\circ} (red)$ .

The gas-phase ML-photodynamics simulations propagated 1,500 trajectories from the  $S_1\text{-FC}$  points for 200 ps with a time step of 0.5 fs. The aggregate-state simulations run 500 trajectories for 20 ps with the same time step. Figure 3A plots the state population dynamics of HPS in the first 40 ps. The  $S_1$  population of HPS showed an exponential  $S_1 \rightarrow S_0$  non-radiative decay in the gas phase when fitting a non-radiative decay rate constant  $k_{nr}$  of  $8.08 \times 10^{10} \ s^{-1}$ . The  $S_1$  population of HPS aggregate showed frequent transitions between  $S_1$  and  $S_2$ , where only 3 trajectories were found in  $S_0$  at the end of simulations. The corresponding  $k_{nr}$  is  $1.66 \times 10^8 \ s^{-1}$ . The predicted  $\alpha_{AIE}=263$  (Equation S7) was in excellent agreement with the experimental results ( $\alpha_{AIE}=255$ ).  $^{34}$  Figure 3B shows the  $S_1$  state populations of TPS, fitting  $k_{nr}=1.23 \times 10^{11}$  and  $2.58 \times 10^{10} \ s^{-1}$  in the gas phase and aggregate, respectively. The predicted AIE factor of TPS ( $\alpha_{AIE}=5$ ) further improved with the previously calculated values ( $\alpha_{AIE}=45$ ) reported by Shuai and co-workers,  $^{34}$  close to the experimental data ( $\alpha_{AIE}=3$ ). Figure 3C illustrates the state populations of COTh, dominated by the  $S_1 \rightarrow S_0$  non-radiative transition. The predicted  $k_{nr}$  of COTh were





 $3.41 \times 10^{11}$  and  $2.87 \times 10^{10}$  s<sup>-1</sup> in the gas phase and aggregate, respectively. These results predicted an AIE factor of COTh ( $\alpha_{AIE} = 12$ ) that exactly matched the experimental results ( $\alpha_{AIE} = 12$ ). Together, the state population dynamics results suggest the reliability of our ML-photodynamics approach for simulating the aggregates. Details on the state populations and the calculations of  $\alpha_{AIE}$  are in gas-phase ML-photodynamics and aggregate ML-photodynamics.

We examined the state population dynamics and found the  $k_{nr}$  of COTh is 3 and 8 times higher than TPS in the gas phase and the aggregate, respectively. These results indicate the  $k_{nr}$  decreases when the AIE molecules are substituted with phenyl groups. We also noted that the  $k_{nr}$  of TPS was close to HPS in the gas phase but was two orders of magnitude faster than those in aggregate. These results suggest the  $k_{nr}$  further decreases with the increasing number of phenyl groups in aggregate. The following discussions will explain how phenyl group motions control the non-radiative decay of HPS and TPS and identify the relevant intramolecular motions responsible for the non-radiative decay of COTh.

### Non-radiative decay mechanisms

We characterize HPS, TPS, and COTh geometries in the gas-phase trajectories using the parameters introduced in Figure 2. The HPS trajectories (Figure 3D) started from the  $S_1$ -FC regions at  $\alpha=48^\circ$  and  $\beta=9^\circ$ . They bifurcate into two pathways along the  $\alpha$  parameter ( $\alpha>0^\circ$  and  $\alpha<0^\circ$ ), indicating two accessible conformations of the phenyl groups instead of random orientations at the  $S_1/S_0$  surface hopping seam. The trajectories feature simultaneous back-and-forth (e.g., fanning) phenyl torsions along with the  $\beta$  axis ( $\beta>0^\circ$  and  $\beta<0^\circ$ ). The concerted phenyl group torsions and silole-core twisting at the  $S_1/S_0$  surface hopping points (Figure S14) resemble the silole-core  $\pi_{CC}$  torsions. We froze the silole core during the gas-phase ML-photodynamics to determine the role of the silole-core  $\pi_{CC}$  torsions. None of the trajectories showed  $S_1/S_0$  surface hopping, while the phenyl groups showed full torsional flexibility (Figure S15). These results suggest that the silole-core  $\pi_{CC}$  torsions were the driving force behind the non-radiative decay of HPS.

Figure 3E plots the structural evolutions of TPS in the gas phase. From the  $S_1\text{-FC}$  regions at  $\alpha=131^\circ$  and  $\beta=-2^\circ$ , the phenyl group rotations slightly increased to  $\alpha=143^\circ$  at  $S_1/S_0$  surface hopping points. The silole core showed strong  $\pi_{CC}$  torsion between  $-100^\circ$  and  $100^\circ$ , while the  $S_1/S_0$  surface hopping points are found in a narrow range from  $-56^\circ$  to  $-30^\circ$ . We observed the concerted phenyl group rotations and silole-core twisting at the  $S_1/S_0$  surface hopping points (Figure S18). These results suggest that the TPS followed a similar non-radiative decay mechanism to HPS, controlled by the silole-core  $\pi_{CC}$  torsions.

The gas-phase trajectories of COTh (Figure 3F) starting at the  $S_1\text{-FC}$  region ( $\gamma=123^\circ$  and  $\theta=0^\circ$ ) showed rapid inversions of  $\gamma$  from  $77^\circ$  to  $283^\circ$ . We found a broad distribution of the  $S_1/S_0$  surface hopping points along each side of  $\gamma=180^\circ$ , which suggests that COTh inversion does not control the  $S_1/S_0$  surface hopping points. The inversion ratio is 39%, corresponding to a decrease of 78% in circular dichroism intensity by single photon absorption. The inversion ratio will converge to 50% upon constant irradiation, showing a gradual reduction of circular dichroism intensity to zero, in accordance with the experiments. The major retention structures of COTh resulted from the preferred  $S_1/S_0$  surface hopping points at  $\gamma=155^\circ$ . Tracking the dihedral angles inside the COTh-core showed concerted  $\pi_{\rm CC}$  torsions (Figure S21). The trajectories displayed strong COTh-core  $\pi_{\rm CC}$  torsions in two opposite directions approaching to  $-90^\circ$  or  $90^\circ$ , where most  $S_1/S_0$  surface hopping points





were located near 36° (Figure 3F). These results indicate that the COTh-core  $\pi_{CC}$  torsions are responsible for the non-radiative decay of COTh.

### Restricted intramolecular motions in aggregates

The gas-phase trajectories of HPS, TPS, and COTh highlighted the unique role of the  $\pi_{CC}$  torsions in the  $S_1 \rightarrow S_0$  non-radiative decay. We continued to explore the relationship between the restrictions of the  $\pi_{CC}$  torsions and the reduced non-radiative decay in the aggregates. We compared the structural distributions of the  $S_1/S_0$  surface hopping structures in 1,500 gas-phase trajectories and 500 aggregate trajectories (Figure 4).

We analyzed the geometries of the trajectories and grouped the structures along the gas-phase  $S_1/S_0$  seam of HPS in Figure 4A, where  $\alpha=121^\circ$  and  $\beta=44^\circ$ . The scatter plot in Figure 4D shows four  $S_1/S_0$  surface hopping regions in the gas phase due to the flexible phenyl rotations and silole-core  $\pi_{CC}$  torsions. By contrast, the HPS aggregates prevented the phenyl rotations and the silole-core  $\pi_{CC}$  torsion. Most trajectories clustered around  $\alpha=35^\circ$  and  $\beta=11^\circ$  in 20 ps in aggregate, near the  $S_1$ -FC regions ( $\alpha=48^\circ$  and  $\beta=8^\circ$ ). We only found three HPS aggregate trajectories that underwent the  $S_1/S_0$  surface hopping at  $\alpha=25^\circ$  and  $\beta=33^\circ$ , which are close to the gas-phase  $S_1/S_0$  surface hopping regions with notable silole-core  $\pi_{CC}$  torsions ( $\beta=44^\circ$ ). This finding implied that the silole-core  $\pi_{CC}$  torsions were still responsible for the non-radiative decay of the HPS in aggregate. The restricted silole-core  $\pi_{CC}$  torsions resulted in a significant reduction of the non-radiative decay of HPS aggregate.

Figure 4B demonstrates the silole-core  $\pi_{CC}$  torsions in the gas-phase  $S_1/S_0$  surface hopping structures of **TPS**. The structural distributions (Figure 4E) suggest an efficient  $S_1/S_0$  surface hopping region at  $\alpha=142^\circ$  and  $\beta=-32^\circ$ . The broad  $S_1/S_0$  surface hopping regions were reduced in aggregate. A few trajectories arrived at the ground state via a narrow region at  $\alpha=139^\circ$  and  $\beta=-26^\circ$  (Figure 4H). Compared with the initial condition ( $\alpha=131^\circ$  and  $\beta=-1^\circ$ ), the phenyl torsions were almost unchanged in aggregate, while the silole-core  $\pi_{CC}$  torsions ( $\beta=-26^\circ$ ) are close to the gas-phase  $S_1/S_0$  surface hopping structures ( $\beta=-32^\circ$ ). These results agreed with our findings in HPS aggregate trajectories; the silole-core  $\pi_{CC}$  torsion controlled the non-radiative decay of the aggregate. Moreover, the non-radiative decay of the TPS aggregate is faster than the HPS aggregate because the silole-core  $\pi_{CC}$  torsion contained flexible hydrogen atoms, whose motions were less restricted than the phenyl groups in the aggregates. Thus, the phenyl groups acted as molecular handles to block the silole-core  $\pi_{CC}$  torsions in the aggregates, deactivating the non-radiative decay.

The gas-phase  $S_1/S_0$  surface hopping structures of COTh depicted a bending COTh-core (Figure 4C). The inversion of COTh should lead to the mirror image of the  $S_1/S_0$  crossing regions relative to the planar COTh ( $\gamma=180^\circ$ ). However, the trajectories showed an uneven distribution, where most  $S_1/S_0$  surface hopping points were found at  $\gamma=153^\circ$  and  $\theta=30^\circ$  (Figure 4F). This dynamical effect drives the trajectories toward a relatively low-energy region of the  $S_1/S_0$  seam near the  $S_1$ -FC regions ( $\gamma=123^\circ$  and  $\theta=0^\circ$ ). The  $S_1/S_0$  surface hopping points showed an elliptical distribution of  $\theta$  from  $-67^\circ$  to  $67^\circ$ , suggesting a crossing seam along with the COTh-core  $\pi_{CC}$  torsions. In aggregate, the inversion angle of COTh decreased to  $\gamma=144^\circ$  at the energetically favorable  $S_1/S_0$  surface hopping region (Figure 4I), which produced no inversion product. The COTh-core  $\pi_{CC}$  torsions showed a reduced range from  $-53^\circ$  to  $48^\circ$ , where the most  $S_1/S_0$  surface hopping points were at  $\theta=15^\circ$ . These





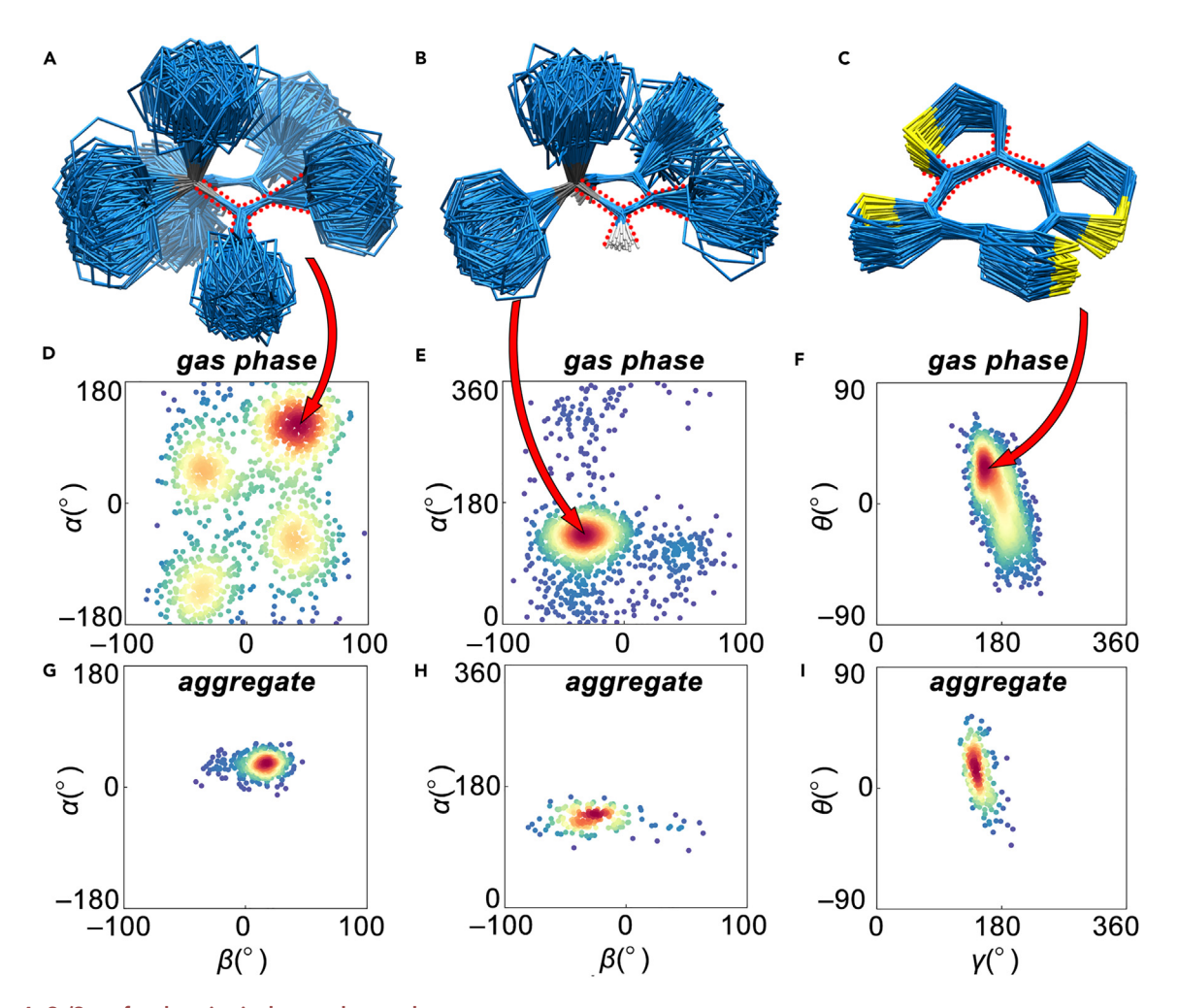


Figure 4.  $\ensuremath{S_1/S_0}$  surface hopping in the gas phase and aggregates

(A-C) Overlay of the selected  $S_1/S_0$  surface hopping structures in the 40 ps gas-phase ML-photodynamics simulations for **HPS**, **TPS**, and **COTh**. The H in the phenyl and thiophene groups is omitted for clarity.

(D–F) Scatter plots for the structural distributions of the gas-phase  $S_1/S_0$  surface hopping points of HPS, TPS, and COTh. The two-dimensional spaces for HPS and TPS are spanned over the phenyl torsion angle ( $\alpha$ ) and silole-core  $\pi_{CC}$  torsion angle ( $\beta$ ); the space for COTh is defined by the inversion angle ( $\gamma$ ) and the COTh-core  $\pi_{CC}$  torsion angle ( $\beta$ ). The ranges of  $\beta$  are  $-82^{\circ}$  to  $98^{\circ}$  and  $-91^{\circ}$  to  $91^{\circ}$  for HPS in (D) and TPS in (E), respectively. The range of  $\theta$  is  $-67^{\circ}$  to  $67^{\circ}$  for COTh in (F).

(G) The structural distributions of HPS in aggregate at the end of the simulations.

(H and I) The structural distributions of the  $S_1/S_0$  surface hopping points of **TPS** and **COTh** in aggregate, respectively. The ranges of  $\beta$  are  $-82^{\circ}$  to  $98^{\circ}$  for **HPS** in (G) and  $-68^{\circ}$  to  $53^{\circ}$  for **TPS** in (H). The range of  $\theta$  is  $-53^{\circ}$  to  $49^{\circ}$  for **COTh** in (I). The color from red to blue describes the accumulation of  $S_1/S_0$  surface hopping structures from high to low, estimated by the Gaussian Kernel.

results confirmed that the COTh-core  $\pi_{CC}$  torsions led to the non-radiative decay of the COTh aggregate.

The magnitudes of the  $\pi_{CC}$  torsions in the  $S_1/S_0$  surface hopping points informed the accessibility of the non-radiative decay pathway of HPS, TPS, and COTh, which reduced from 178°, 182°, and 133° in the gas phase (Figures 4D–4F) to 92°, 144°, and 102° in aggregate (Figures 4G–4I), respectively. The reduction ratios were 48%, 21%, and 23%, which indicate the decreasing restriction on the non-radiative decay in HPS>COTh>TPS. This trend explained the decreasing order of the predicted  $\alpha_{AlE}$  in TPS(5)<COTh(12)<HPS(263). These findings revealed the role of phenyl groups as molecular handles that conveyed intermolecular steric clashes in





aggregates into intramolecular restrictions on the silole-core  $\pi_{CC}$  torsions, deactivating the non-radiative decay. Without adequate molecular handles, TPS or COTh could not sufficiently harness the intermolecular interactions to restrict the intramolecular  $\pi_{CC}$  torsion in the conjugated core, which led to a weak AIE phenomenon.

### **Conclusions**

We used the ML-photodynamics simulations based on a combination of NNs trained with QM data, semiempirical methods, and molecular mechanics to investigate the non-radiative decay mechanisms of typical AIE molecules, HPS, TPS, and COTh. The simulations provided high-fidelity structural information to reveal the contributions of restricted intramolecular motions in the non-radiative decay pathways in aggregates.

The excited-state population analysis predicted the AIE factors of HPS (263), TPS (5), and COTh (12) in line with the experiments. The  $S_1/S_0$  surface hopping distributions showed the non-radiative decay originated from notable silole-core  $\pi_{CC}$  torsions in HPS ( $\beta=44^\circ$ ) and TPS ( $\beta=-32^\circ$ ) in the gas phase instead of the phenyl group rotations. The trajectories of COTh showed that the excited-state inversions are independent of the non-radiative decay, where the COTh-core  $\pi_{CC}$  torsions ( $\theta=28^\circ$ ) promoted the  $S_1/S_0$  surface hopping. The trajectory analysis showed a decrease in intermolecular restrictions of the  $\pi_{CC}$  torsions as follows HPS>COTh>TPS in their aggregates, which explained the decreasing trend in the predicted AIE factors. These findings revealed the actual role of phenyl groups as molecular handles to hinder the excited-state  $\pi_{CC}$  torsions.

Understanding the non-radiative decay mechanism of typical AIE molecules is one step forward toward the rational design of AIE materials. The ML-photodynamics simulations suggest a simple design rule for the organic AIE molecules by introducing bulky or rigid substituent groups at or near the  $\pi_{\rm CC}$ -bonds. The substituents act as molecular handles to harness the intermolecular steric hindrances and clashes to resist the excited-state  $\pi_{\rm CC}$  torsions in the aggregates, leading to AIE.

### **EXPERIMENTAL PROCEDURES**

### Resource availability

### Lead contact

Further information and requests for resources should be directed to and will be fulfilled by the lead contact, Jingbai Li (lijingbai@szpu.edu.cn).

### Materials availability

This study did not generate new unique reagents

### Data and code availability

- The ML-photodynamics simulation code is open-sourced and released at: https://github.com/mlcclab/PyRAI2MD-hiam.
- The NN models and initial conditions generated during this study are available at: https://github.com/mlcclab/PyRAI2MD\_publications/AIE\_project.
- The training data and full initial conditions are available upon request to the lead contact.

### **Model preparations**

For gas-phase models, we optimized the geometries of HPS, TPS, and COTh with the PBE0/cc-pVDZ method. Wigner sampling was used to sample the





non-equilibrium geometries in the gas phase at the zero-point energy level. For aggregate models, we created a 4×4×3 supercell for HPS, TPS, and COTh from the unit cell (CCDC: 195948, 933864, 606349). We then applied a cutoff radius ( $R_{cut-}$ off) to select two crystal shells. The R<sub>cutoff</sub> of HPS, TPS, and COTh are 17, 15, and 14 Å, which contained 27, 30, and 33 molecules, respectively. Then, we replaced the central molecule inside the crystal shells with 500 Wigner-sampled non-equilibrium geometries. We froze the non-equilibrium geometries and initial velocities at the center and relaxed the crystal shells. The relaxations started with the GFN-FF dynamics in 1 ps and switched to hybrid GFN0-xTB/GFN-FF dynamics for another 400 ps. The time step was 1 fs. The hybrid GFN0-xTB/GFN-FF calculations first computed the energy of the whole aggregate model with the GFN-FF method. Then, it replaced the GFN-FF energy of the inner shell with the GFN0-xTB results. The initial velocities of atoms in the crystal shells are randomly generated following the Boltzmann distribution at 298 K. The translational and rotational velocities are projected out. We confined the radius to 21.86, 27.30, and 18.34 Å for the HPS, TPS, and COTh aggregates to mimic the solvent-solute repulsions packing the isolated molecule into aggregates. The GFN0-xTB and GFN-FF calculations used the program xTB 6.5.1.<sup>55,56</sup>

### Multiscale approach

We partitioned the aggregate models into three layers: core, inner shell, and outer shell. The HPS, TPS, and COTh aggregates have 11, 11, and 13 molecules in the inner shells and 15, 18, and 19 molecules in the outer shell, respectively. The total energy was expressed using the subtractive ONIOM scheme:

$$E_{\text{total}} = E_{\text{GFN-FF,model}} - E_{\text{GFN-FF,inner+center}} + E_{\text{GFN0-xTB,inner+center}} - E_{\text{GFN0-xTB,center}} + E_{\text{NN,center}}$$

where the  $E_{GFN-FF,model}$  term is the GFN-FF energy of the whole aggregate model.  $E_{GFN-FF,inner+center}$ , and  $E_{GFN0-xTB,inner+center}$  terms are the GFN-FF and GFN0-xTB energies of the inner shells, including the molecule at the center. The  $E_{GFN0-xTB,center}$ , and  $E_{NN,center}$  terms are the GFN0-xTB and NN-predicted energies of the central molecule. As HPS, TPS, and COTh are neutral and apolar, the polarizations from the inner shell to the center were weak. The TD- $\omega$ B97XD/cc-pVDZ calculations suggest a mean absolute difference of 0.01–0.02 eV between the gas-phase excitation energies and that with embedding charges of the inner shell (Figure S6). Thus, we computed the  $E_{GFN0-xTB,center}$ , and  $E_{NN,center}$  terms in the gas phase for simplicity and accounted for the interaction between the center and inner shell in the  $E_{GFN0-xTB,inner+center}$  term.

Further error analyses were discussed in error analysis. The nuclear forces are negative first-order derivatives of the above total energy function with respect to the nuclear positions. The three-layer ONIOM scheme was implemented in  $PvRAI^2MD$ .

### Quantum mechanical calculations

The ground-state geometries of HPS, TPS, and COTh were optimized with the PBE0/cc-pVDZ method. The excited-state calculations used the  $\omega$ B97XD/cc-pVDZ. The predicted excitation energies of HPS, TPS, and COTh were 3.67, 4.36, and 4.03 eV, which agreed with the experiment results, 3.42, 4.31, and 3.64 eV.<sup>25,58,59</sup> The predicted emission energies of HPS, TPS, and COTh were 2.65, 2.77, and 2.11 eV in line with the measure data, 2.49, 2.94, and 2.46 eV.<sup>25,58,59</sup> The simulated absorption spectra (Figure S2) suggest the lowest accessible excited state was S<sub>1</sub>.





The photodynamics simulations for the non-radiative  $S_1 \rightarrow S_0$  transitions require multireference methods, such as CASPT2, to correctly describe the PESs near the crossing regions. To date, the CASPT2 calculations for AIE molecules remain computationally infeasible. The CASSCF method is a second choice as it is less resource-intensive than CASPT2, while it often overestimates the excitation energies due to the lack of dynamical electron correlations. Our benchmarks showed the energy calculations for HPS with the SA2-CASSCF(4,4)/ANO-S-VDZP method spent more than 2 h. Reducing the basis set to the minimal set (SA2-CASSCF(4,4)/ANO-S-MB) still took 4 h to obtain the  $S_1$  and  $S_0$  energies and forces. For HPS, the simulation time will be 18 years as the notable non-radiative decay occurred in 20 ps according to the rate constant (2.53 ×  $10^{10}$  s<sup>-1</sup>) reported by Shuai and coworkers. Thus, to the best of our knowledge, ML-photodynamics is one of the few available methods to simulate the non-radiative decay of HPS, TPS, and COTh aggregates.

The SA2-CASSCF(4,4)/ANO-S-MB method was unsuitable for training data calculations because of the poor data quality with the minimal basis set and the lack of dynamical electron correlations, although the computational cost seemed affordable. We compared the TD- $\omega$ B97XD/cc-pVDZ method to SA2-CASSCF(4,4)/ANO-S-MB at the  $S_1/S_0$ -MECIs. The TD- $\omega$ B97XD/cc-pVDZ calculations showed comparable optimized structures, g (gradient difference), and h(nonadiabatic coupling) vectors to the CASSCF(4,4)/ANO-S-MB reference. The reference for COTh was computed with the CASSCF(8,8)/ANO-S-MB method (Figure S3). A well-known issue of TDDFT calculations is the missing dimensionality of the branching plane. 47,48 Here, the discrepancy in the PESs became less significant when the  $S_1$ – $S_0$  energy gap was > 0.3 eV. It was because the  $S_1$ / $S_0$ -MECIs were sloped, and the gradient difference dominated the molecular vibrations that lifted the  $S_1/S_0$  degeneracy. Thus, the  $TD-\omega B97XD/cc-pVDZ$  method was reliable if the structures were not at the  $S_1/S_0$ -MECIs, which was a fair assumption for HPS, TPS, and COTh because more than 90% of S<sub>1</sub>/S<sub>0</sub>-surface hopping events attempted to occur with an  $S_1$ - $S_0$  energy gap > 0.3 eV (Figure S11). The initial training sets excluded the data at or near the  $S_1/S_0$ -MECIs (i.e.,  $S_1-S_0$ gap < 0.3 eV). The TD- $\omega$ B97XD/cc-pVDZ, energy, and force calculations were finished in 40 min. The PBE0/cc-pVDZ and  $TD-\omega B97XD/cc-pVDZ$ calculations used ORCA 5.0.3.60 The CASSCF calculations used OpenMolcas 19.11.61 Detailed discussions on the QM methods are available in quantum mechanical calculations.

### Training data generation

The initial training data contained two parts: Wigner sampling and geometric interpolation. We performed Wigner sampling based on the PBE0/cc-pVDZ optimized geometries to generate 800 HPS, TPS, and COTh structures at the zero-point energy level, respectively. The geometric interpolation generated 22 structures for HPS and 20 structures for TPS and COTh from the  $S_1$ -FC point to the  $S_1$ / $S_0$  crossing points (Figure S4). We only kept 18 structures in the middle of the interpolations to remove duplicated data at the  $S_1$ -FC point and incorrect data at the  $S_1$ / $S_0$  crossing points. Then, the interpolated geometries were perturbed by the nuclear displacements obtained from another 100 Wigner-sampled structures for HPS and 50 Wigner-sampled structures for TPS and COTh, which produced 1,800, 900, and 900 data points for HPS, TPS, and COTh. The total numbers of data in the initial set were 2,600, 1,700, and 1,700 for HPS, TPS, and COTh, respectively. The training data contain the  $S_0$ ,  $S_1$ , and  $S_2$  energies and gradients. The training data were split into training and validation sets in a 9:1 ratio.





We performed adaptive sampling to expand the initial training set with undersampled data. The adaptive sampling used a committee model of two NNs to propagate 100 trajectories from the  $S_1$  state for 10 ps with a step size of 0.5 fs. The standard deviation (STD) in the predicted energy and gradients by the NN committee indicate the uncertainty of the current prediction. The trajectories were stopped if the STD exceeded the empirical thresholds for energy (0.03 Hartree) or gradients (0.08 Bohr • Hartree  $^{-1}$ ), respectively. The last geometries of the stopped trajectories were recomputed with the TD- $\omega$ B97XD/cc-pVDZ calculations and added to the initial training set. After that, the adaptive sampling retrained the committee model of NNs to restart the trajectories until no out-of-sampled structure was found. Detailed information on the adaptive sampling is available in adaptive sampling.

### **ML-photodynamics simulations**

The ML-photodynamics simulations used a feed-forward NN consisting of multiple Perceptron layers based on the TensorFlow/Keras API for Python. <sup>62</sup> The NN computes the inverse distance matrix of the input molecule to predict the energies and gradients. The NN employed a leaky softplus activation function. The energies and forces are trained using a combined loss function with a ratio of 5:1 to ensure their physical relationship. The hyperparameters were optimized by a grid search over 378 NNs. The mean absolute errors in the NN-predicted energies were 0.0135–0.0147, 0.0265–0.0343, and 0.0214–0.0293 eV for HPS, TPS, and COTh, respectively. The optimized hyperparameters and detailed information on the NN errors are available in neural network potential.

We propagated the 1,500 gas-phase and 500 aggregate-state trajectories from the  $S_1$ -FC points of HPS and TPS. The simulation times were 200 ps in the gas phase and 20 ps in aggregate. The time step was 0.5 fs. The probability of a nonadiabatic electronic transition was computed with Tully's FSSH method, 51,52 where we used the curvature-driven time-derivative coupling (kTDC) method  $^{49,50}$  to evaluate the NACs based on the NN-predicted energy gaps. The kTDC method showed a good accuracy to the ground-truth NAC obtained with QM calculations when the energy gap was sufficiently small (e.g., 0.5 eV). 53,54 Our NNs tended to predict the  $S_1/S_0$  surface hopping at  $S_1-S_0$  energy gap > 0.3 eV as the data with smaller gaps were excluded. Thus, the ML-photodynamics simulations overestimated the rate constants of the non-radiative decay. We benchmarked the  $S_1\!-\!S_0$  energy gap to determine the magnitude of the kTDC overestimation of the exact NAC. Based on our results, we applied the  $S_1$ – $S_0$  energy gap threshold of 2.05, 2.0, and 1.0 eV to evaluate the kTDC for HPS, TPS, and COTh, which overestimated the NAC 2-10 times (Figure S5). Since the gas-phase and aggregate-state simulation used the same NN models, the overestimations of the non-radiative decay rate constants were canceled out in the AIE factor, which did not significantly affect the predicted AIE factors. Detailed discussions on the kTDC benchmarks are available in quantum mechanical calculations.

### SUPPLEMENTAL INFORMATION

Supplemental information can be found online at https://doi.org/10.1016/j.chempr. 2024.04.017.

### **ACKNOWLEDGMENTS**

J.L. acknowledges the funding support provided by the Research Foundation of Shenzhen Polytechnic University Research under grant 6023312036K. L.W. and





J.L. thank the support of the high-performance computing resources at the Hoffmann Institute of Advanced Materials at Shenzhen Polytechnic University. S.A.L. acknowledges the NSF (NSF-CHE-2144556) for funding. J.L. and S.A.L. appreciate the assistance from the Northeastern Research Computing Team and the computing resources provided by the Massachusetts Life Science Center grant (G00006360).

### **AUTHOR CONTRIBUTIONS**

J.L. conceptualized the project. L.W. performed the TDDFT calculations, NN training, and ML-photodynamics simulations under the supervision of J.L. C.S. performed the CASSCF calculations under the supervision of S.A.L. L.W., C.S., and J.L. analyzed the data. L.W. and J.L. wrote the manuscript. All authors revised the manuscripts. J.L. and S.A.L. acquired the financial support for the project.

### **DECLARATION OF INTERESTS**

The authors declare no competing interests.

Received: February 6, 2024 Revised: April 17, 2024 Accepted: April 24, 2024 Published: May 14, 2024

### **REFERENCES**

- Ha, J.M., Hur, S.H., Pathak, A., Jeong, J.-E., and Woo, H.Y. (2021). Recent advances in organic luminescent materials with narrowband emission. NPG Asia Mater. 13, 1–36. https:// doi.org/10.1038/s41427-021-00318-8.
- Sun, W., Guo, S., Hu, C., Fan, J., and Peng, X. (2016). Recent Development of Chemosensors Based on Cyanine Platforms. Chem. Rev. 116, 7768–7817. https://doi.org/10.1021/acs. chemrev.6b00001.
- Krämer, J., Kang, R., Grimm, L.M., De Cola, L., Picchetti, P., and Biedermann, F. (2022). Molecular Probes, Chemosensors, and Nanosensors for Optical Detection of Biorelevant Molecules and Ions in Aqueous Media and Biofluids. Chem. Rev. 122, 3459– 3636. https://doi.org/10.1021/acs.chemrev. 1c00746.
- Mako, T.L., Racicot, J.M., and Levine, M. (2019). Supramolecular Luminescent Sensors. Chem. Rev. 119, 322–477. https://doi.org/10.1021/acs. chemrev.8b00260.
- Cao, D., Liu, Z., Verwilst, P., Koo, S., Jangjili, P., Kim, J.S., and Lin, W. (2019). Coumarin-Based Small-Molecule Fluorescent Chemosensors. Chem. Rev. 119, 10403–10519. https://doi.org/ 10.1021/acs.chemrev.9b00145.
- Ma, J., Shu, T., Sun, Y., Zhou, X., Ren, C., Su, L., and Zhang, X. (2022). Luminescent Covalent Organic Frameworks for Biosensing and Bioimaging Applications. Small 18, e2103516. https://doi.org/10.1002/smll.202103516.
- 7. Yang, M., Guo, X., Mou, F., and Guan, J. (2023). Lighting up Micro-/Nanorobots with Fluorescence. Chem. Rev. 123, 3944–3975. https://doi.org/10.1021/acs.chemrev.2c00062.
- 8. Xing, Z., Wu, W., Miao, Y., Tang, Y., Zhou, Y., Zheng, L., Fu, Y., Song, Z., and Peng, Y. (2021). Recent advances in quinazolinones as an

- emerging molecular platform for luminescent materials and bioimaging. Org. Chem. Front. 8, 1867–1889. https://doi.org/10.1039/ DOQO01425G.
- Ambiliraj, D.B., Francis, B., and Reddy, M.L.P. (2022). Lysosome-targeting luminescent lanthanide complexes: from molecular design to bioimaging. Dalton Trans. 51, 7748–7762. https://doi.org/10.1039/D2DT00128D.
- Yang, Y., Zhao, Q., Feng, W., and Li, F. (2013). Luminescent Chemodosimeters for Bioimaging. Chem. Rev. 113, 192–270. https:// doi.org/10.1021/cr2004103.
- Boeije, Y., and Olivucci, M. (2023). From a onemode to a multi-mode understanding of conical intersection mediated ultrafast organic photochemical reactions. Chem. Soc. Rev. 52, 2643–2687. https://doi.org/10.1039/ D2C.500719C.
- Wang, H., Li, Q., Alam, P., Bai, H., Bhalla, V., Bryce, M.R., Cao, M., Chen, C., Chen, S., Chen, X., et al. (2023). Aggregation-Induced Emission (AIE), Life and Health. ACS Nano 17, 14347– 14405. https://doi.org/10.1021/acsnano. 3c03925.
- Mei, J., Leung, N.L.C., Kwok, R.T.K., Lam, J.W.Y., and Tang, B.Z. (2015). Aggregation-Induced Emission: Together We Shine, United We Soar! Chem. Rev. 115, 11718–11940. https://doi.org/10.1021/acs.chemrev.5b00263.
- 14. Yang, H., Zheng, J., Xie, M., Luo, D., Tang, W.-J., Peng, S.-K., Cheng, G., Zhang, X., Zhou, X.-P., Che, C.-M., et al. (2022). Aggregation-Enhanced Emission in a Red Cu(I) Emitter with Quantum Yield >99%. ACS Materials Lett. 4, 1921–1928. https://doi.org/10.1021/acsmaterialslett.2c00661.
- 15. Wang, D., and Tang, B.Z. (2019). Aggregation-Induced Emission Luminogens for Activity-

- Based Sensing. Acc. Chem. Res. *52*, 2559–2570. https://doi.org/10.1021/acs.accounts. 9b00305.
- Zhang, Z., Huang, Y., Bai, Q., Wu, T., Jiang, Z., Su, H., Zong, Y., Wang, M., Su, P.-Y., Xie, T.-Z., et al. (2022). Aggregation-Induced Emission Metallocuboctahedra for White Light Devices. JACS Au 2, 2809–2820. https://doi.org/10. 1021/jacsau.2c00568.
- Liu, J., Huang, W., Liang, B., Chen, Y., Liu, Y., Zhang, X., Zheng, S., Zhu, L., Feng, S., and Huang, W. (2022). C3-Symmetric Propeller-like Phenanthridine Derivative with Multiple Write-In Modes for Programmable Anti-Counterfeiting. Chem. Mater. 34, 9492–9502. https://doi.org/10.1021/acs.chemmater. 201942.
- Ma, J., Gu, Y., Ma, D., Lu, W., and Qiu, J. (2022). Insights into AIE materials: A focus on biomedical applications of fluorescence. Front. Chem. 10, 985578. https://doi.org/10.3389/ fchem.2022.985578.
- Han, P., Lin, C., Xu, H., Xia, E., Yang, D., Qin, A., Ma, D., and Tang, B.Z. (2022). Improving the Efficiency of AlEgen-Based Nondoped Blue Organic Light-Emitting Diode by Rational Isomer Engineering. ACS Materials Lett. 4, 1087–1093. https://doi.org/10.1021/ acsmaterialslett.2c00344.
- Zhu, J., and Jiang, X. (2024). How does aggregation-induced emission aggregate interdisciplinary research? Aggregate 5, e451. https://doi.org/10.1002/agt2.451.
- Dini, V.A., Genovese, D., Micheletti, C., Zaccheroni, N., Pucci, A., and Gualandi, C. (2023). Emission or scattering? Discriminating the origin of responsiveness in AlEgen-doped smart polymers using the TPE dye. Aggregate 4, e373. https://doi.org/10.1002/agt2.373.

# **Chem** Article



- Leung, N.L.C., Xie, N., Yuan, W., Liu, Y., Wu, Q., Peng, Q., Miao, Q., Lam, J.W.Y., and Tang, B.Z. (2014). Restriction of Intramolecular Motions: The General Mechanism behind Aggregation-Induced Emission. Chemistry 20, 15349–15353. https://doi.org/10.1002/chem.201403811.
- Zhang, H., Zhao, Z., Turley, A.T., Wang, L., McGonigal, P.R., Tu, Y., Li, Y., Wang, Z., Kwok, R.T.K., Lam, J.W.Y., and Tang, B.Z. (2020). Aggregate Science: From Structures to Properties. Adv. Mater. 32, e2001457. https://doi.org/10.1002/adma. 202001457.
- Mei, J., Hong, Y., Lam, J.W.Y., Qin, A., Tang, Y., and Tang, B.Z. (2014). Aggregation-Induced Emission: The Whole Is More Brilliant than the Parts. Adv. Mater. 26, 5429–5479. https://doi. org/10.1002/adma.201401356.
- Tang, B.Z., Zhan, X., Yu, G., Sze Lee, P.P.S., Liu, Y., and Zhu, D. (2001). Efficient blue emission from siloles. J. Mater. Chem. 11, 2974–2978. https://doi.org/10.1039/B102221K.
- Chen, J., Law, C.C.W., Lam, J.W.Y., Dong, Y., Lo, S.M.F., Williams, I.D., Zhu, D., and Tang, B.Z. (2003). Synthesis, Light Emission, Nanoaggregation, and Restricted Intramolecular Rotation of 1,1-Substituted 2,3,4,5-Tetraphenylsiloles. Chem. Mater. 15, 1535–1546. https://doi.org/10.1021/ cm021715z.
- Zhang, G.-F., Chen, Z.-Q., Aldred, M.P., Hu, Z., Chen, T., Huang, Z., Meng, X., and Zhu, M.-Q. (2014). Direct validation of the restriction of intramolecular rotation hypothesis via the synthesis of novel orthomethyl substituted tetraphenylethenes and their application in cell imaging. Chem. Commun. (Camb) 50, 12058–12060. https://doi.org/10.1039/C4CC04241G.
- Yuan, C.-X., Tao, X.-T., Ren, Y., Li, Y., Yang, J.-X., Yu, W.-T., Wang, L., and Jiang, M.-H. (2007). Synthesis, Structure, and Aggregation-Induced Emission of a Novel Lambda (Δ)-Shaped Pyridinium Salt Based on Tröger's Base. J. Phys. Chem. C 111, 12811–12816. https://doi.org/10.1021/ip0/11601.
- Li, Q., and Blancafort, L. (2013). A conical intersection model to explain aggregation induced emission in diphenyl dibenzofulvene. Chem. Commun. (Camb) 49, 5966–5968. https://doi.org/10.1039/ c3cc41730a.
- Peng, X.-L., Ruiz-Barragan, S., Li, Z.-S., Li, Q.-S., and Blancafort, L. (2016). Restricted access to a conical intersection to explain aggregation induced emission in dimethyl tetraphenylsilole.
  J. Mater. Chem. C 4, 2802–2810. https://doi. org/10.1039/C5TC03322E.
- Crespo-Otero, R., Li, Q., and Blancafort, L. (2019). Exploring Potential Energy Surfaces for Aggregation-Induced Emission—From Solution to Crystal. Chem. Asian J. 14, 700–714. https://doi.org/10.1002/asia. 201801649.
- Peng, Q., and Shuai, Z. (2021). Molecular mechanism of aggregation-induced emission. Aggregate 2. https://doi.org/10.1002/ agt2.91.

- Pieri, E., Lahana, D., Chang, A.M., Aldaz, C.R., Thompson, K.C., and Martínez, T.J. (2021). The non-adiabatic nanoreactor: towards the automated discovery of photochemistry. Chem. Sci. 12, 7294–7307. https://doi.org/10. 1039/D15C00775K.
- Xie, Y., Zhang, T., Li, Z., Peng, Q., Yi, Y., and Shuai, Z. (2015). Influences of Conjugation Extent on the Aggregation-Induced Emission Quantum Efficiency in Silole Derivatives: A Computational Study. Chem. Asian J. 10, 2154–2161. https://doi.org/10.1002/asia. 20150303
- Zhao, Z., Zheng, X., Du, L., Xiong, Y., He, W., Gao, X., Li, C., Liu, Y., Xu, B., Zhang, J., et al. (2019). Non-aromatic annulene-based aggregation-induced emission system via aromaticity reversal process. Nat. Commun. 10, 2952. https://doi.org/10.1038/s41467-019-10818-5
- Crespo-Otero, R., and Barbatti, M. (2018). Recent Advances and Perspectives on Nonadiabatic Mixed Quantum-Classical Dynamics. Chem. Rev. 118, 7026–7068. https://doi.org/10.1021/acs.chemrev. 7b00577
- Nelson, T.R., White, A.J., Bjorgaard, J.A., Sifain, A.E., Zhang, Y., Nebgen, B., Fernandez-Alberti, S., Mozyrsky, D., Roitberg, A.E., and Tretiak, S. (2020). Non-adiabatic Excited-State Molecular Dynamics: Theory and Applications for Modeling Photophysics in Extended Molecular Materials. Chem. Rev. 120, 2215– 2287. https://doi.org/10.1021/acs.chemrev. 9b00447.
- Zobel, J.P., and González, L. (2021). The Quest to Simulate Excited-State Dynamics of Transition Metal Complexes. JACS Au 1, 1116–1140. https://doi.org/10.1021/jacsau. 1c00252.
- Prlj, A., Došlić, N., and Corminboeuf, C. (2016). How does tetraphenylethylene relax from its excited states? Phys. Chem. Chem. Phys. 18, 11606–11609. https://doi.org/10.1039/ C5CP04546K.
- Gao, X., Peng, Q., Niu, Y., Wang, D., and Shuai, Z. (2012). Theoretical insight into the aggregation induced emission phenomena of diphenyldibenzofulvene: a nonadiabatic molecular dynamics study. Phys. Chem. Chem. Phys. 14, 14207–14216. https://doi.org/10. 1039/C2CP40347A.
- Dral, P.O., and Barbatti, M. (2021). Molecular excited states through a machine learning lens. Nat. Rev. Chem. 5, 388–405. https://doi.org/10. 1038/s41570-021-00278-1.
- Westermayr, J., and Marquetand, P. (2021). Machine Learning for Electronically Excited States of Molecules. Chem. Rev. 121, 9873– 9926. https://doi.org/10.1021/acs.chemrev. 0c00749.
- Li, J., and Lopez, S.A. (2023). Machine learning accelerated photodynamics simulations. Chem. Phys. Rev. 4, 031309. https://doi.org/10. 1063/5.0159247.
- 44. Westermayr, J., Gastegger, M., Vörös, D., Panzenboeck, L., Joerg, F., González, L., and Marquetand, P. (2022). Deep learning study of tyrosine reveals that roaming can lead to photodamage. Nat. Chem. 14,

- 914–919. https://doi.org/10.1038/s41557-022-00950-z.
- Westermayr, J., Gastegger, M., Menger, M.F.S.J., Mai, S., González, L., and Marquetand, P. (2019). Machine learning enables long time scale molecular photodynamics simulations. Chem. Sci. 10, 8100–8107. https://doi.org/10.1039/ C9SC01742A.
- Zheng, X., Peng, Q., Zhu, L., Xie, Y., Huang, X., and Shuai, Z. (2016). Unraveling the aggregation effect on amorphous phase AIE luminogens: a computational study. Nanoscale 8, 15173–15180. https://doi.org/10.1039/ C6NR03599.1.
- Huix-Rotllant, M., Nikiforov, A., Thiel, W., and Filatov, M. (2016). Description of Conical Intersections with Density Functional Methods. Density-Functional Methods for Excited States, N. Ferré, M. Filatov, and M. Huix-Rotllant, eds. (Springer), pp. 445–476. https://doi.org/10. 1007/128\_2015\_631.
- Levine, B.G., Ko, C., Quenneville, J., and Martínez, T.J. (2006). Conical intersections and double excitations in time-dependent density functional theory. Mol. Phys. 104, 1039–1051. https://doi.org/10.1080/ 00268970500417762.
- Shu, Y., Zhang, L., Chen, X., Sun, S., Huang, Y., and Truhlar, D.G. (2022). Nonadiabatic Dynamics Algorithms with Only Potential Energies and Gradients: Curvature-Driven Coherent Switching with Decay of Mixing and Curvature-Driven Trajectory Surface Hopping. J. Chem. Theory Comput. 18, 1320–1328. https://doi.org/10.1021/acs.jctc. 1c01080.
- Zhao, X., Merritt, I.C.D., Lei, R., Shu, Y., Jacquemin, D., Zhang, L., Xu, X., Vacher, M., and Truhlar, D.G. (2023). Nonadiabatic Coupling in Trajectory Surface Hopping: Accurate Time Derivative Couplings by the Curvature-Driven Approximation. J. Chem. Theory Comput. 19, 6577–6588. https://doi. org/10.1021/acs.jctc.3c00813.
- Tully, J.C. (1990). Molecular dynamics with electronic transitions. J. Chem. Phys. 93, 1061–1071. https://doi.org/10.1063/1. 459170.
- Hammes-Schiffer, S., and Tully, J.C. (1994). Proton transfer in solution: Molecular dynamics with quantum transitions. J. Chem. Phys. 101, 4657–4667. https://doi.org/10. 1063/1.467455.
- Do Casal, T., Toldo, J.M., Pinheiro, M., and Barbatti, M., Jr. (2021). Fewest switches surface hopping with Baeck-An couplings. Open Res. Europe 1, 49. https://doi.org/10.12688/ openreseurope.13624.1.
- Merritt, I.C.D., Jacquemin, D., and Vacher, M. (2023). Nonadiabatic Coupling in Trajectory Surface Hopping: How Approximations Impact Excited-State Reaction Dynamics. J. Chem. Theory Comput. 19, 1827–1842. https://doi.org/10. 1021/acs.jctc.2c00968.
- Bannwarth, C., Ehlert, S., and Grimme, S. (2019). GFN2-xTB—An Accurate and Broadly Parametrized Self-Consistent Tight-Binding Quantum Chemical Method with Multipole





- Electrostatics and Density-Dependent Dispersion Contributions. J. Chem. Theory Comput. 15, 1652–1671. https://doi.org/10. 1021/acs.jctc.8b01176.
- Spicher, S., and Grimme, S. (2020). Robust Atomistic Modeling of Materials, Organometallic, and Biochemical Systems. Angew. Chem. Int. Ed. Engl. 59, 15665– 15673. https://doi.org/10.1002/anie. 202004239.
- 57. Li, J., Reiser, P., Boswell, B.R., Eberhard, A., Burns, N.Z., Friederich, P., and Lopez, S.A. (2021). Automatic discovery of photoisomerization mechanisms with nanosecond machine learning photodynamics simulations. Chem. Sci. 12,

- 5302–5314. https://doi.org/10.1039/ D0SC05610C.
- 58. Zhao, E., Lam, J.W.Y., Hong, Y., Liu, J., Peng, Q., Hao, J., Sung, H.H.Y., Williams, I.D., and Tang, B.Z. (2013). How do substituents affect silole emission? J. Mater. Chem. C 1, 5661–5668. https://doi.org/10.1039/C3TC30880D.
- Ji, Z., Zhao, C., Zhang, C., Wang, Z., Ma, Z., Xu, L., and Wang, H. (2023). Synthesis and AIE properties of benzene fused cyclooctetrathiophenes. J. Photochem. Photobiol. A 436, 114362. https://doi.org/10. 1016/j.jphotochem.2022.114362.
- 60. Neese, F. (2022). Software update: The ORCA program system—Version 5.0. WIREs Comput.

- Mol. Sci. 12, 1–15. https://doi.org/10.1002/wcms.1606.
- 61. Fdez Galván, I., Vacher, M., Alavi, A., Angeli, C., Aquilante, F., Autschbach, J., Bao, J.J., Bokarev, S.I., Bogdanov, N.A., Carlson, R.K., et al. (2019). OpenMolcas: From Source Code to Insight. J. Chem. Theory Comput. 15, 5925–5964. https://doi.org/10.1021/acs.jctc.9b00532.
- 62. Abadi, M., Agarwal, A., Barham, P., Brevdo, E., Chen, Z., Citro, C., Corrado, G.S., Davis, A., Dean, J., Devin, M., et al. (2016). TensorFlow: Large-Scale Machine Learning on Heterogeneous Distributed Systems. Preprint at arXiv. available from tensorflow.org.